Real-time microsecond dynamics of single biomolecules probed by plasmon-enhanced fluorescence

Sjoerd W. Nooteboom*[1,2], Kasper R. Okholm*[3,4], Vincenzo Lamberti[1,2], Bas Oomen[1,2], Duncan S. Sutherland†[3,4], and Peter Zijlstra†[1,2]

[1]Department of Applied Physics and Science Education, Eindhoven University of Technology, 5600 MB Eindhoven, The Netherlands

[2]Institute for Complex Molecular Systems, Eindhoven University of Technology, 5600 MB Eindhoven, The Netherlands

[3]Interdisciplinary Nanoscience Center, Aarhus University, 8000 Aarhus C, Denmark

[4]The Centre for Cellular Signal Patterns (CELLPAT), 8000 Aarhus C, Denmark

Abstract

Biomolecules exhibit dynamics on widely varying timescales, which are critical to their functioning in living systems. Particularly sub-millisecond dynamics, such as low-affinity ligand binding and interactions of individual binding sites within multivalent complexes, remain elusive. These dynamics are typically probed in real-time using single-molecule fluorescence, but photophysics limits it to millisecond timescales. Here, we exploit and optimize the strong plasmonic fluorescence enhancement provided by monocrystalline gold nanoparticles to detect $> 10^7$ photons/s from single fluorophores. The ultrahigh signals uniquely enable real-time single-molecule fluorescence studies with 1-10 μs temporal resolution, and single-molecule correlation spectroscopy within < 1 s. We use this method to reveal molecular diffusion and ultralow-affinity DNA interactions on microsecond timescales. We further exploit the field gradient around the nanoparticles to reveal dynamic binding transitions of multivalently binding Holliday junctions. Our results pave the way towards real-time microsecond studies of biomolecular complexes using an implementation compatible with existing single-molecule fluorescence methods.

*These authors contributed equally.
†Corresponding author

Main

Biomolecules such as nucleic acids and proteins form the functional basis of all living organisms. Their functionality originates from dynamic processes such as folding, conformational changes, and intermolecular interactions. Prime examples are the conformational changes and interaction dynamics of enzymes [1, 2], intrinsically disordered proteins (IDPs) [3, 4], nucleic acids [5, 6], and cellular receptors [7]. Critically, many biomolecular interactions are multivalent where a stronger bond is accomplished by combining multiple low-affinity (and thus dynamic) bonds [8]. All these processes span a very broad range of timescales from picoseconds to hours [9, 10]. A combination of molecular dynamics simulations and ensemble-averaged studies has revealed that such fast dynamics are crucial for the biological function, while misregulation of the dynamics can lead to disease due to e.g. misfolding [11] or aberrant interaction thermodynamics [12]. Overall, understanding the mechanisms of biomolecular dynamics on all relevant timescales is key to progress in molecular biology and medicine.

Biomolecular dynamics are often studied in solution where fluorescence correlation spectroscopy resolves dynamics down to nanoseconds by averaging over many single-molecule passages through a focused laser beam. However, such ensemble-averaging methods hide underlying static and dynamic heterogeneity despite its importance for function and disease [13, 14]. Real-time single-molecule fluorescence of immobilized biomolecules directly reveals dynamics and heterogeneity in time, and has provided a wealth of information on molecular mechanisms of *e.g.* DNA [15, 16] and proteins [14, 17–20]. However, the brightness of a fluorophore saturates at a photon count rate (PCR) of about 10^5 photons/s, so sub-ms timescales can again only be obtained by averaging over hundreds to thousands of single molecules (which typically takes minutes or hours) to obtain a sufficient signal-to-noise ratio [21, 22].

Our understanding of fast biomolecular dynamics therefore mainly comes from atomistic molecular dynamics simulations that provide access to timescales ranging from femto- to microseconds [23]. Recent experiments have provided the first direct look into real-time microsecond dynamics using label-free detection based on plasmonic nanopores [24], Fabry-Pérot microcavities [25], or interferometric scattering microscopy [26]. Label-free techniques usually do not suffer from signal saturation, but their lack of chemical specificity restricts their usage to the probing of molecular diffusion [24–26]. A recent pioneering study employed plasmon-enhanced fluorescence and reported the use of polycrystalline plasmonic nano-apertures [27] to enhance the PCR of single fluorophores to approximately 10^6 photons/s. This study showed the promise of using nanoplasmonic approaches to boost fluorophore brightness, but remains to be applied to biomolecular processes. Experimental access to microsecond dynamics of single biomolecules therefore remains elusive but of critical importance to get insight into fast processes and enable comparison to molecular simulations.

Here, we use the fluorescence enhancement provided by single-crystalline gold nanoparticles to further push the fluorescence intensity of single organic fluorophores, by an order of magnitude above state of the art levels. A synergistic combination of antenna optimization and suppression of blinking provides a PCR of more than 10^7 photons/s for a single organic dye conjugated to single-stranded DNA. We used this to study single-

molecule interactions of ultralow affinity, for the first time resolving DNA diffusion and ultralow-affinity DNA hybridization in real-time on timescales of 1-10 μs. We further exploit the strong gradient in fluorescence enhancement around the nanoparticle to directly reveal the dynamic binding transitions of individual binding sites in a bivalent construct. We observe strong heterogeneity in the dynamics due to local differences in the density (effective concentration [28]) of receptors. Our method is compatible with any commercial fluorescence microscope and therefore expands the utility of single-molecule fluorescence toward microsecond processes and beyond.

Optimization of photon count rates

Plasmon-enhanced fluorescence modifies the fluorescence intensity by two distinct mechanisms. On the one hand the highly confined and enhanced local electric field around a plasmonic nanoparticle increases the excitation rate of nearby emitters. On the other hand, the coupling of the emitter's emission dipole to the plasmon enhances the radiative and nonradiative decay rates of the emitter. The total enhancement factor in the weak excitation regime (below saturation) is a combination of these two effects and depends on the intrinsic quantum yield of the dye [29]. This means that very high enhancement factors can be reached for dyes with a poor quantum yield; indeed enhancement factors of up to 5000 have been reported [30]. For short-timescale studies, though, the enhancement factor itself is not meaningful; rather, it is crucial to maximize the absolute PCR. This requires a high excitation rate (close to saturation), in combination with an enhanced radiative decay rate that increases the saturation intensity [31, 32].

To maximize the absolute PCR we chose gold nanorods (AuNRs) as the core geometry since they can be synthesized colloidally with high purity in single-crystalline form [33, 34]. The latter is crucial as the elimination of defects improves the fluorescence enhancement compared to lithographic structures due to reduced plasmon dephasing [35]. In addition, the localized surface plasmon resonance (LSPR) of AuNRs was tuned to a nominal value of 650 nm, away from the interband transitions in gold [36, 37]. The AuNRs were immobilized on a glass slide at low density and functionalized with thiolated single-stranded DNA receptors (see Methods and Fig. 1a-b). The sample was inserted in a flow cell and mounted on a standard fluorescence microscope with 637 nm laser excitation. Ligand (monovalent or multivalent) labelled with Atto655 was introduced in the flow cell, resulting in transient single-molecule interactions with the receptor strands on the particle. The single-molecule interactions were detected on a camera for millisecond temporal resolution, or on a single-photon counting avalanche photodiode (SPAD) for microsecond measurements (see Methods for a detailed description of the microscopy). Fig. 1c contains an exemplary timetrace showing short-lived bursts of plasmon-enhanced fluorescence due to 9 nucleotide (nt) ligand interactions that are superimposed on a stable baseline due to the particle's one-photon luminescence [32, 38].

In order to quantify the plasmon-enhanced PCR we applied a threshold to each timetrace for automated event detection (see Methods). We then selected the 10 brightest events in each timetrace, which are representative

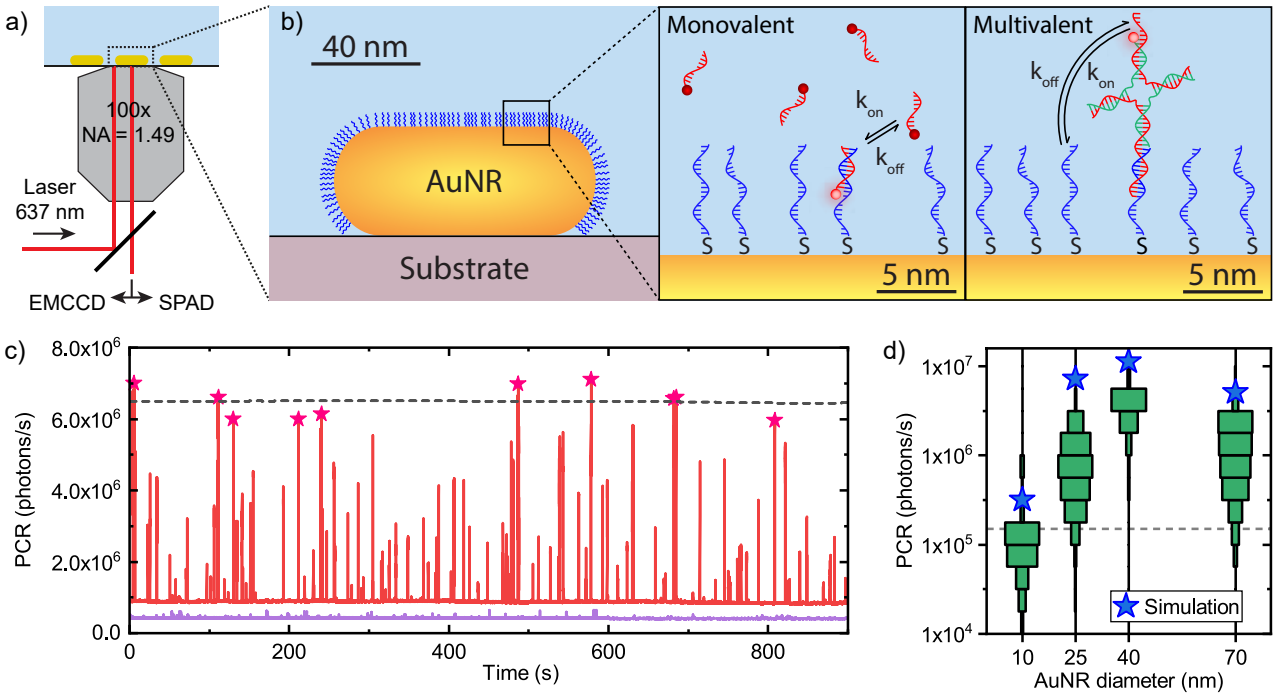

Figure 1: a) Schematic illustration of the setup used in this work. The sample consists of AuNRs that were spin coated on a glass coverslip at low density, mounted in a flow cell. Single-molecule fluorescence signals were detected on an electron-multiplying charge coupled device (EMCCD) for millisecond dynamics, or on a SPAD for microsecond dynamics. b) The gold particles are functionalized with thiolated single-stranded DNA receptor strands (blue). The introduction of monovalent or bivalent ligands results in transient single-molecule interactions with characteristic rate constants k_{on} and k_{off} (note that the indicates rates have different values depending on the ligand). c) An example fluorescence timetrace of monovalent ssDNA ligands transiently interacting with a single AuNR recorded on the camera (red) compared to the background signal (blue). The 10 brightest events are highlighted by red stars, the dashed line indicates their average PCR. d) Distribution of obtained PCR values of the top 10 bursts as a function of AuNR diameter: experimental data (green histograms) and simulated maxima for each AuNR diameter (blue stars). The grey line indicates the nonenhanced PCR.

of the binding events near the tips of the particle, where the fluorescence enhancement is maximized [39]. To maximize the PCR we studied the effect of the AuNR diameter on the signals, keeping the average LSPR constant around 650 nm. The results are aggregated across all single AuNRs in the field-of-view, see Fig. 1d. For every AuNR diameter, we observe a distribution of intensities indicating particle-to-particle differences in maximum PCR. This is due to the varying distance of each AuNR from the center of the Gaussian laser beam (affecting the local excitation intensity) and to the heterogeneous LSPR wavelengths (affecting the spectral overlap with the excitation and emission wavelengths).

The PCR as a function of AuNR diameter follows a clear trend, with the 40 nm diameter AuNRs providing the highest enhancement. If the excitation intensity is well beyond the saturation point, the PCR is dictated by the radiative decay rate k_r. According to the simulations, the k_r enhancement is nearly independent of nanoparticle size for diameters of $\geq$ 25 nm (see Supplementary Figure S1-5 for details of the simulations). In this size regime the higher radiative efficiency of larger nanoantennas is compensated for by a broader plasmon linewidth caused by radiation damping (see Supplementary Figure S6-7 for experimental plasmon linewidths). This means that at or above saturation the PCR is nearly diameter-independent in our intermediate size regime.

In the experiments however we do observe a dependence of the PCR on nanoantenna diameter, indicating that we operate just below saturation where the excitation rate is maximum for 40 nm AuNRs due to their high near-field enhancement and low nonradiative losses [40]. Indeed, the measured PCR is close to the values found from simulations neglecting saturation (see the blue stars in Fig. 1d). For our further experiments we selected the 40 nm AuNRs since nearly all particles in this batch exhibited a PCR close to 10^7 photons/s, providing access to integration times in the low microsecond regime.

We optimized the combination of dye and buffer conditions to minimize dark states due to *e.g.* triplet dynamics. The high PCR uniquely enables us to quantify microsecond blinking dynamics in real-time by projecting the signal from a single particle onto a SPAD that enables arbitrary time-binning. The middle left panel in Fig. 2a shows the start of a typical event for a 9nt ligand with an Atto655 label pointing toward the nanoparticle surface as in Fig. 1b. Clear dark states are observed with durations ranging from 10 μs to $>$ 10 ms, while the dye spends on average 32% of the time in a dark state. We find better signal stability for an Atto643 label pointing outward into solution, possibly due to a better photostability of the fluorophore. Upon adding Trolox, a well-known triplet state quencher [41], the observed off-blinks become markedly shorter. To further reduce the duration of dark states we employed a mixed monolayer of ssDNA receptors and shorter ssDNA spacers to maximize the accessibility of the dye to solution-phase Trolox. In this case, off-blinks lasting longer than 200 μs are virtually eliminated, while the dye (on average) spends only 6% of its time in a dark state (see the right column in Fig. 2a).

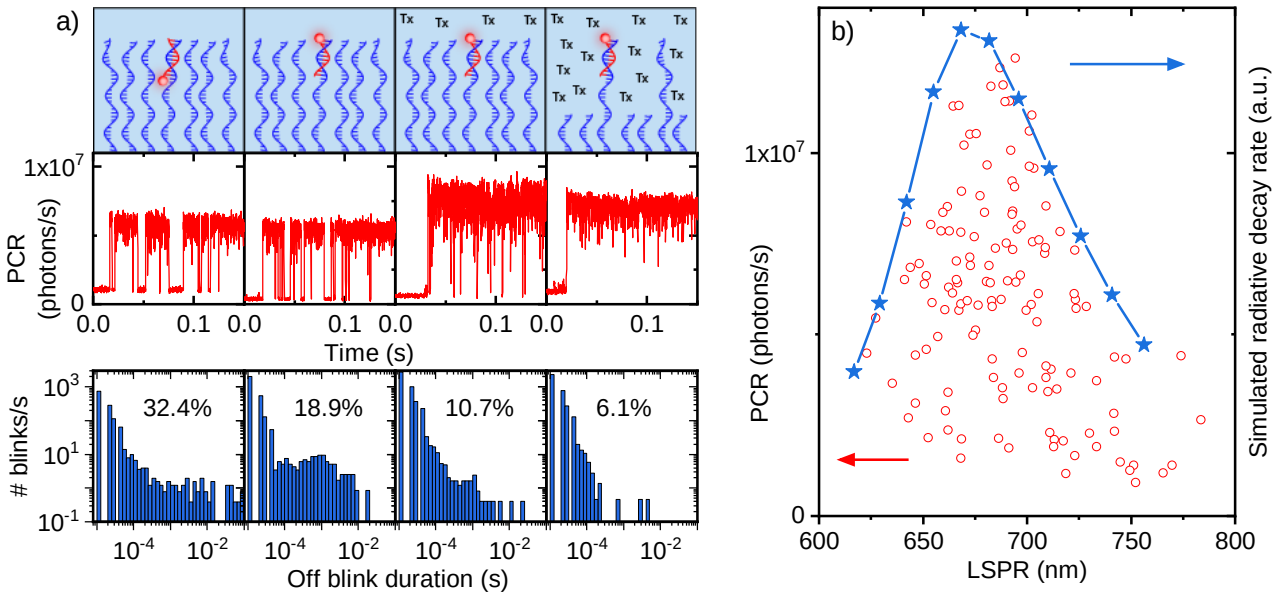

Figure 2: a) Top: schematic comparison of the DNA micro-environment corresponding to the results below: Atto655 inward; Atto643 outward; Atto643 with 2 mM Trolox (Tx); Atto643 with 2 mM Trolox in a mixed monolayer of ssDNA receptors and spacer strands. Middle: representative events with 100 μs binning time, illustrating the reduction of blinking. Bottom: the number of blinks per second as a function of off blink duration under the four different conditions, obtained from 10 μs binned timetraces. The percentages indicate the fraction of time the dye spends in the dark state. b) PCR as a function of LSPR for the top 10 bursts, for the conditions in the right column of a). Each data point indicates a single AuNR in the field of view. The blue stars indicate the simulated enhancement of the radiative decay rate as a function of LSPR.

Using the optimized AuNR dimensions and buffer conditions we quantified the PCR in a widefield measurement on the EMCCD to acquire statistics across many single AuNRs. The PCR of the ten brightest events on a collection of individual AuNRs is plotted versus their LSPR in Fig. 2b. Many AuNRs yield single-molecule PCRs around 10^7 photons/s, thereby providing access to low microsecond binning times with 10-100 photons per time bin. The shape of the envelope closely resembles the LSPR dependence of the k_r enhancement, rather than the overall (unsaturated) fluorescence enhancement. This implies that the current experimental conditions are in a regime close to saturation of Atto643.

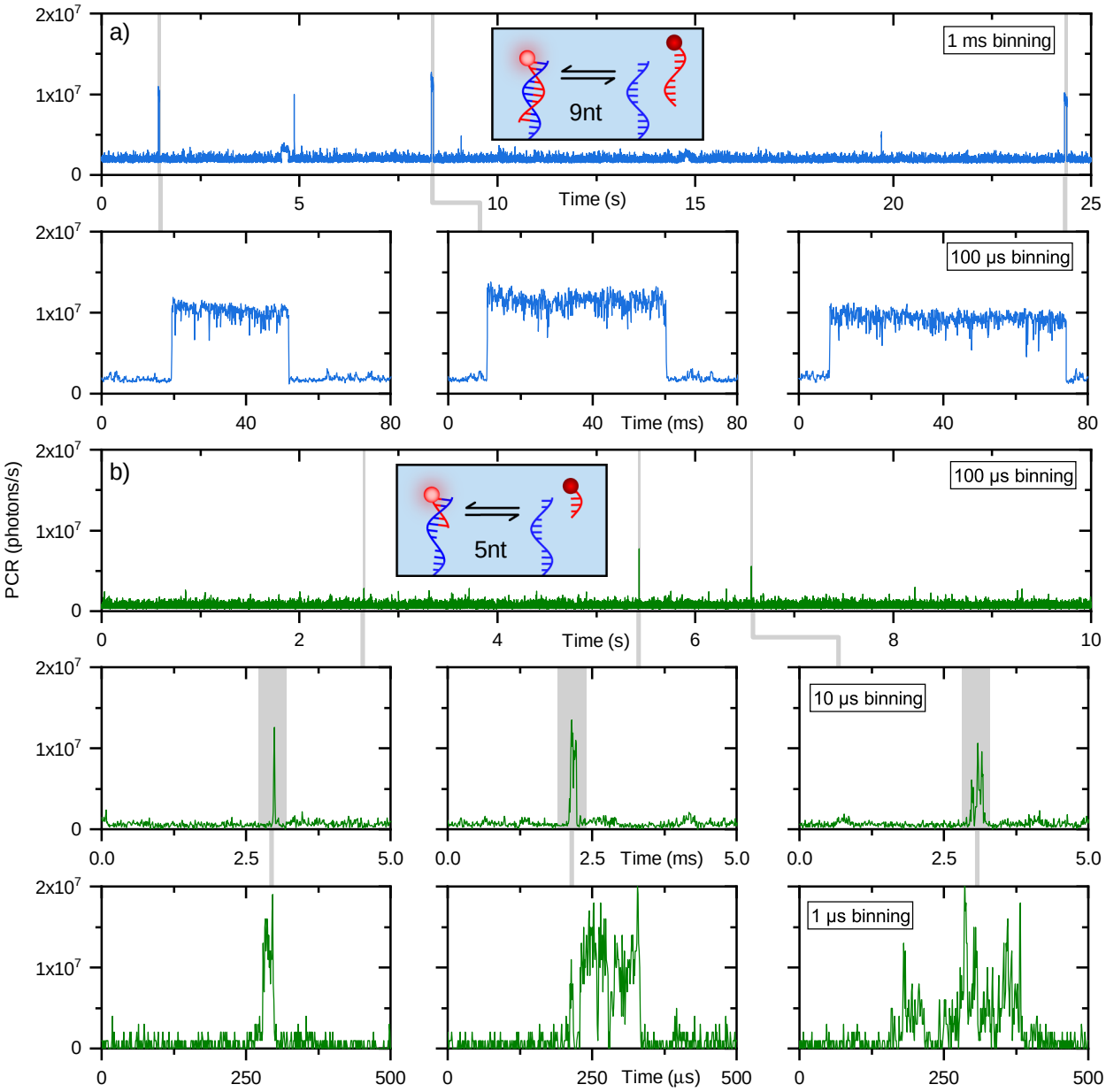

Figure 3: Successive zoom-ins of timetraces with 9nt (a) and 5nt (b) ligands. The wider panels show timetraces lasting many seconds. Grey areas indicate the regions that are shown as a zoom on the next row with decreased binning time (see the binning times in the legend of each row). Experimental conditions were as described in the Methods section.

Ultrafast dynamics of monovalent ligands

The synergistic optimization of nanoantenna, buffer, and dye opens the window to study real-time microsecond dynamics of biomolecular interactions. Fig. 3a shows a part of a timetrace for 9nt ligands that diffuse and transiently hybridize with complementary strands on the particle's surface. Timetraces are shown for 1 ms and 100 μs binning, revealing transient interactions with high signal-to-noise ratio. Bound-state lifetimes are on the order of tens of ms (see further discussion below), dictated by the sequence, buffer conditions, and local temperature. Fig. 3b shows the same experiment for much shorter 5nt interactions. Strikingly, most events are so short-lived that even at 100 μs binning they are nearly undetectable. 10 μs binning is necessary to resolve the events, but even at 1 μs binning the signal-to-noise ratio is sufficient to clearly observe transient dynamics. With this binning time, the fluorescence intensities of $1 - 2 \times 10^7$ photons/s correspond to $10 - 20$ photons per bin, with a luminescence background of the AuNR of 1 photon per bin. On 1 μs timescales we observe clear fluctuations in the signal, which are unlikely to be caused by blinking because (with a few exceptions) the fluctuations do not drop to baseline level. We hypothesize that the receptor strand itself changes conformation, thereby modulating the distance and orientation of the dye with respect to the AuNR. More examples of events for different ligands are shown in Supplementary Figures S8-10.

The real-time observation of DNA binding events down to microsecond timescales allows us to straightforwardly quantify the bound-state lifetime even for ultralow affinity interactions. To this end, we repeated the experiments described above for ligands with complementarity between $5 - 9$ nt and used a thresholding algorithm to quantify the distribution of bound-state lifetimes (see Methods for more details). We then fitted the cumulative distribution function (CDF) for each AuNR with a double exponential, yielding two distinct dissociation rates k_{off}. Fig. 4a shows this for one AuNR per ligand (see more examples in Supplementary Figure S11). Repeating this analysis for a larger number of AuNRs, we obtain a distribution of characteristic times k_{off}^{-1} as shown in Fig. 4b. The spread in characteristic times among AuNRs is likely due to photothermal heating, which occurs to a different extent for each AuNR depending on the different LSPR peak wavelengths and orientations; in our setup we expect AuNR surface temperatures around 305 K [42]. However, the difference in bound-state lifetime between ligands of different length is substantially larger than the particle-to-particle variability with the same ligand. The slow component of the double exponential fit changes by nearly three orders of magnitude from 60 ms (median) for 9nt to 150 μs for 5nt ligands. We conclude that the slow component represents biomolecular binding between receptor strands and ligands, representing approximately 10% of all detected events. The change in bound-state lifetime from 5nt to 6nt is an order of magnitude due to the addition of a C/G pair, whereas the relative changes between the longer ligands are factors of $2 - 5$ due to the addition of lower-affinity A/T pairs [43, 44].

The fast component represents approximately 90% of the events with a duration that is nearly constant at about 9 μs across all ligand lengths. Moreover, the same timescale is found for a noncomplementary ligand (*i.e.*, one with no more than 2nt complementarity to the receptor strand, see the leftmost trace in the inset to Fig. 4a).

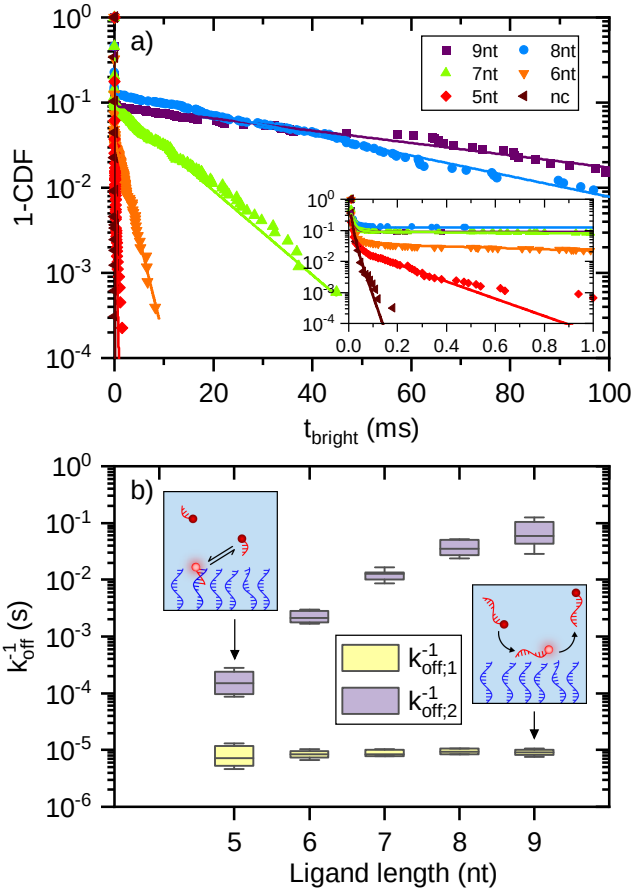

Figure 4: a) Bright time distributions (t_{bright} is the duration of individual events) extracted from individual timetraces with ligands of different lengths, as well as the noncomplementary (nc) control. Each distribution is based on 600-4500 events. Inset: zoom-in to the first millisecond of the same data. b) Spread of characteristic time values obtained from double exponential fits to the distributions as shown in (a). Yellow, fast component; purple, slow component. Boxes indicate 25-75 percentiles with the median line; whiskers indicate 10-90 percentiles. For each ligand, between 12-20 AuNRs were measured.

This component cannot be explained by false positives because the threshold for event detection is well above the Poisson noise level of the baseline PCR. Estimating a hydrodynamic radius of 1 nm for our ligand strands [45], we find a diffusion coefficient of 260 $\mu m^2/s$ at 300 K, so the ligands would diffuse approximately 50 nm, comparable to the size of the AuNR, in 10 μs. The fast component thus corresponds to diffusion of the ligand through the near-field of the AuNR. Access to these very short timescales thereby reveals that mass transport brings the ligands into the near-field of the AuNR leading to an average 10% probability of hybridization. This also opens up possibilities for future detailed studies into the hybridization process.

Ultrafast dynamics of multivalent ligands

The above interactions exhibit a single contiguous binding site, which we dub monovalent. Multivalency however is an abundant principle in nature, where multiple simultaneous low affinity interactions lead to a multivalent interaction with moderate or high affinity referred to as avidity [46, 47]. Additionally, it allows for effects like super selectivity, where multivalent bonds are formed much more effectively above a critical receptor density [48].

Ensemble-averaged approaches have revealed a strong dependency of overall interaction strength on the receptor density and affinity of individual binding sites [46, 47]. Investigating effects of the micro-environment, which can lead to intermolecular heterogeneity, requires a single-molecule technique instead. However, any information about the underlying binding transitions remains hidden because these occur on very short timescales that are inaccessible by conventional single-molecule approaches.

We set out to isolate and study dynamic interactions within a multivalent binding event. As a model system for multivalent interactions we use a bivalent Holliday junction (HJ) [5] (see the sequences in Supplementary Table S1). One arm of the HJ is conjugated to an Atto643 dye that generates a plasmon-enhanced fluorescence signal. We employ three different designs that all exhibit one arm with a binding site of 12nt complementarity, resulting in relatively long binding events (typically ∼1 s). The first HJ with no binding motif on the dye-carrying arm is monovalent (12-only), where the dye-carrying arm diffuses freely in the bound state (Fig. 5a, left column). Here the dye's time-averaged distance to the AuNR is expected to be (nearly) constant (see further discussion in Supplementary Section S5), and its plasmon-enhanced fluorescence intensity is indeed stable in time (Fig. 5a). Note that typical event intensities are somewhat lower than for the simple monovalent ligands (as in Fig.

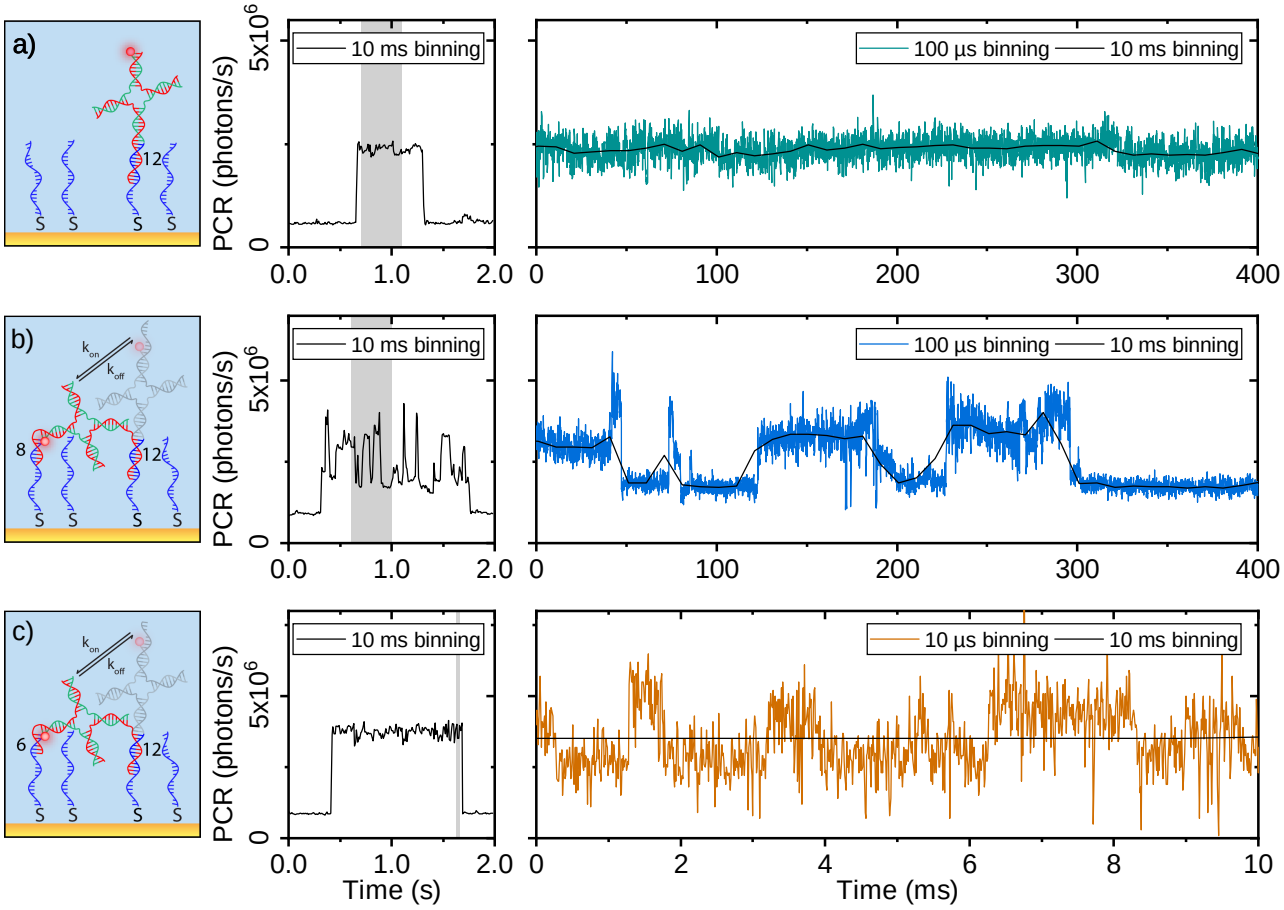

Figure 5: Intensity timetraces of events recorded with three different HJ constructs: a) 12-only, b) 12+8, c) 12+6. Black traces are binned to 10 ms. The right column shows a zoom of the same data binned to 100 μs (a,b) or 10 μs (c). Grey areas highlight the parts enlarged in the right panels. Schematic illustrations of the three HJ constructs are shown to the left of the timetraces.

3) reflecting the larger spacing between the dye and the AuNR surface for the HJ.

The other two HJ constructs (12+8 and 12+6) are bivalent and have an extension at the dye-carrying arm with 8nt or 6nt complementarity to the receptor strands (see Fig. 5b-c, left column). The use of two different strength binding motifs within one bivalent construct allows the kinetic separation of the two binding arms. During a binding event, repeated transient interactions of the second binding site will change the dye-AuNR distance from approximately 13 nm (monovalent state) to approximately 6 nm (bivalent state; see Supplementary Section S6 for a quantification of these estimates). This results in rapid changes in PCR on timescales depending on the affinity of the binding site, because the dye's position is modulated in the rapidly decaying near-field of the AuNR. For this system we used only receptor strands on the AuNR (no spacers) to increase the effective concentration of receptors and the likelihood of bivalent binding.

With a 10 ms binning time, a standard value for single-molecule fluorescence, it is clear that the 12-only construct barely shows dynamics, while the 12+8 exhibits relatively slow dynamics. The 12+6 signal is relatively noisy at this timescale, hinting at dynamics that are too fast to resolve. Zooming in and decreasing the binning time to 100 μs (Fig. 5a-b, right panels), we clearly observe that the 12-only signal is stable and the 12+8 fluctuates on timescales of tens of ms, the fluctuations of the latter being visible in greater detail than before. For the 12+6 we require 10 μs binning to resolve the transient binding events of the bivalent construct because the interactions occur on sub-ms timescales. For most HJs the intensity changes between the mono- and bivalent bound state are around 20-50 percent (see more examples in Supplementary Figures S13-15), which is caused by dynamic changes in dye-nanoparticle spacing. Assuming that the dye is excited to saturation, numerical simulations predict approximately a factor of two difference in fluorescence intensity between the mono- and bivalent bound state, in good agreement with the experiments (see Supplementary Figure S4 for a comparison to simulations).

We observe a small subset of HJs that exhibit clear two-level timetraces (as in Fig. 5c). State lifetimes can be extracted from such timetraces by change-point detection [49] to resolve the time points at which the HJ switches between mono- and bivalent states with a different PCR. The results of this analysis for a selection of events are shown in Supplementary Figure S17. The analysis reveals single-exponentially distributed state lifetimes of a few ms, indicating the involvement of one or more binding sites with similar association and dissociation rates and PCRs. The majority of events however exhibits complex multi-state dynamics because the low-affinity binding site can bind to multiple receptor strands on the particle surface (as in Fig. 5b, also see the examples in Supplementary Figures S14-15). We therefore computed the autocorrelation function (ACF) of the PCR of many single binding events. This approach is analogous to fluorescence correlation spectroscopy (FCS), but does not average the dynamics over many events as is done in regular FCS. Instead, we extract the dynamics within a single event, representing state-switching of a single molecule during the event that lasts on the order of $0.1 - 1$ s.

The ACFs corresponding to the events in Fig. 5 are shown in Fig 6a (see more examples in Supplementary Figure S16). All ACFs exhibit a characteristic decay time with low amplitude on the order of 10 μs which we

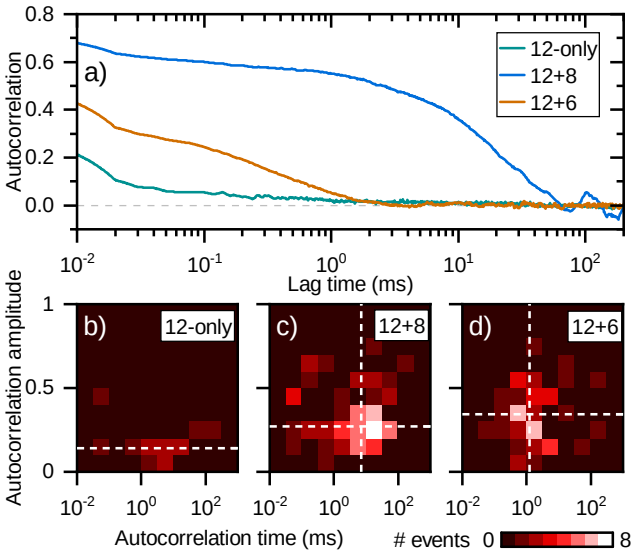

Figure 6: a) Autocorrelation functions computed from the timetraces shown in Fig. 5, based on 10 μs binning. b-d) Heat maps of the fitted characteristic time versus amplitude of the ACFs computed from all individual events of the different HJs. White dashed lines indicate the median autocorrelation time and amplitude.

attribute to residual blinking. Apart from this, the ACF of the 12-only construct has a very low correlation amplitude because the monovalent HJ cannot switch to a bivalent state, resulting in a nearly stable PCR during the event. The 12+8 and 12+6 ACFs show significantly higher amplitudes, matching the more dynamic signals visible from the timetraces. The most prominent timescale in the 12+8 construct's ACF is on the order of 10 ms, whereas the lower affinity 12+6 construct switches on a timescale of a few hundred μs.

To quantify the dynamics of the different constructs, we fitted the ACFs of all the HJ events using a stretched exponential function (see Supplementary Section S9 for more details). Since all ACFs exhibit a small component of $\sim$10 μs, we fitted the curves starting from 40 μs. In Fig. 6b-d we show heat maps of the characteristic time versus the ACF amplitude. The amplitudes for the 12-only are low for nearly all events (median 0.14), indicating a nearly stable PCR. On the other hand, the median ACF amplitudes for 12+8 and 12+6 are 0.27 and 0.34, respectively, with many individual events showing much higher amplitudes up to 0.75 indicating significant signal fluctuations - *i.e.* switching between monovalent and bivalent bound states. The median characteristic time for the 12+8 is 7.0 ms, whereas the 12+6 has a median characteristic time of 1.2 ms. This reduction in characteristic timescale is similar to the difference in bright time between the monovalent 8nt and 6nt ligands as described above (see further discussion in Supplementary Section S9).

Interestingly, the characteristic times are broadly distributed for both the 12+8 and 12+6 constructs. We hypothesize that the receptor layer on the AuNR is heterogeneous in density, thereby modulating the accessibility of nearby receptors for the second binding site. Hence the HJ will sometimes be unable to switch between the monovalent and bivalent states, or it will switch with varying rates depending on the local availability (effective concentration) of binding sites. For the 12+8 HJ we find a weak correlation between the total bound-state lifetime (event duration) and the characteristic time in the ACF. This indicates that the overall affinity of the

complex is slightly enhanced by more stable bivalent binding, but dominated by the 12nt binding site. The ability to directly observe fast multivalent dynamics and its heterogeneity is unique and will enable the rational design of multivalent substrates [50] and the characterization of multivalent interactions on heterogeneous surfaces such as lipid bilayers [18, 51].

Conclusion

In summary, by synergistic optimization of gold nanoantennas, surface functionalization, and buffer conditions we push the PCR of single organic fluorophores to $> 10^7$ photons/s. With the current diffusion-based triplet quenching system, the accessibility of the dye to the quencher was shown to play a major role in the triplet quenching rate and suppression of blinking. We demonstrated the utility of such ultrahigh PCRs, combined with the strong field gradients, to probe inter- and intramolecular dynamics in real-time with low-μs temporal resolution. The μs resolution enables the probing of very fast switching between states with different valency, allowing us to isolate and study the dynamic binding transitions within a multivalent bond. We find heterogeneity in the dynamics that is normally hidden in the ensemble average, caused by local variations in accessibility of receptors.

Importantly, the technique is simple, requiring only basic sample preparation steps and a standard fluorescence microscope. The main requirements for the biomolecular system are that a receptor molecule is present near the plasmonic nanoantenna and that the ligand is fluorescently tagged. We envision that this method can be used to study the microsecond dynamics of enzymes, IDPs, or even more complex biomolecular systems at the single-molecule level in real-time. An intriguing possibility is the investigation of highly mobile receptors inside a lipid bilayer. Our method thus opens the door to mechanistic studies of conformationally controlled biomolecular processes via a single-molecule approach in the relevant but previously inaccessible microsecond regime.

Acknowledgements

This project has received funding from the European Union's Horizon 2020 research and innovation programme under the Marie Skłodowska-Curie grant agreement No 860914, and from the Danish National Research Foundation center grant CellPAT (DNRF135). The authors further acknowledge funding from ERC MultiSense and the SuperCol consortium. We also thank Max Bergkamp for providing the change-point detection script.

Methods

Sample preparation. Microscope coverslips (thickness #1.5, Epredia) were cleaned by sonication in methanol for 15 min, then dried by nitrogen flow. The coverslips were plasma-treated for 1 min to render the surface

hydrophilic. They were then immersed in a 5 vol% solution of 3-mercaptopropyltrimethoxysilane (MPTMS) in ethanol for 3 min to create a monolayer of thiols by silanization, followed by rinsing with ethanol and drying by nitrogen flow.

Suspensions of AuNRs of different sizes (NanoPartz) were centrifuged at 10k rpm for 3 min and the supernatant replaced by a 1 mM solution of cetyltrimethylammonium bromide (CTAB) in distilled water. The resulting suspension was spin coated onto the coverslips, which were then rinsed with methanol, phosphate buffered saline (PBS) and distilled water to remove excess CTAB and unbound AuNRs, and dried by nitrogen flow.

Stick-on flow cells (Grace Bio-Labs) were attached to the AuNR-containing glass slides. A solution of 5 μM thiolated ssDNA ($2-100\%$ receptor strands, the remaining part spacer strands; Integrated DNA Technologies) and 1 mM tris(2-carboxyethyl)phosphine hydrochloride (TCEP, Merck) in citrate buffer (10 mM, pH 3, 1 M NaCl) was injected and incubated for ~ 2 h to form a ssDNA monolayer on the AuNRs [52]. All DNA sequences can be found in Supplementary Table S1. Afterwards, the flow cells were rinsed with 200 μL PBS and 200 μL buffer B (5 mM Tris-HCl, 10 mM $MgCl_2$, 1 mM EDTA, pH 8.0, filtered) and stored in the fridge for $1-10$ days before use.

Single-AuNR dark-field spectroscopy Single-AuNR scattering spectra were measured by objective-type total internal reflection microscopy on an inverted wide-field microscope (Nikon Ti2). The sample was illuminated by a collimated SuperK COMPACT supercontinuum laser (NKT Photonics) through an oil-immersion 1.49 NA objective. The excitation wavelength was tuned across the visible spectrum by an AOTF (SuperK Varia) with a bandwidth of 10 nm. A beam block was inserted into the objective's back aperture to block the direct reflection, while allowing the scattered light to pass through and reach an EMCCD camera (Andor iXon Ultra DU-888). The nanoparticle's point spread function (PSF) was fitted with a 2D Gaussian function to obtain the scattered intensity at each wavelength. The single-particle scattering spectrum was fitted with a Lorentzian (see Supplementary Figure S6). AuNRs with an abnormally broad spectrum or a poor fit were excluded from the analysis.

Experimental procedure for widefield fluorescence microscopy. DNA ligands with Atto655 (Eurofins Genomics) were diluted to concentrations between $0.2-1$ nM in buffer B and flushed into the sample chamber. The sample was illuminated by a 637 nm excitation laser (OBIS FP 637LX, Coherent). A quarter waveplate (Thorlabs) was used to achieve circular polarization and the sample was illuminated in epi mode to eliminate the effect of different AuNR orientations. The laser power density in the center of the field of view was approximately 10^8 W/m^2. The reflected laser light was suppressed by combining a dichroic mirror (ZT640rdc, Chroma), a notch filter (ZET635NF, Chroma), and a long-pass filter (FELH0650, Thorlabs) and the fluorescence signal was collected on the same camera used for the scattering spectra with a 50 ms exposure time.

Fluorescence timetraces were constructed by summing the pixel values of 7x7 regions of interest (ROIs) around the AuNRs, and converted to photons/s by dividing by the camera sensitivity (in A/D counts per photon, provided by the manufacturer) and exposure time. To obtain the PCR from the fluorescence events in the timetraces, the background due to the nanoparticle's one-photon photoluminescence was first removed by a

moving median filter. Bursts were then identified by application of a threshold. Events with a maximum of 2 dark frames between them were merged. For the nonenhanced PCR, the same procedure was repeated on ROIs near the center of the field of view without AuNRs in them and the highest bursts were averaged over ~ 100 ROIs.

Experimental procedure for microsecond single-molecule dynamics. Trolox (Merck) was dissolved in ethanol at a concentration of 160 mM. It was then diluted to 2 mM in imaging buffer (5 mM Tris-HCl, 300 mM NaCl, 1 mM EDTA, pH 8.0, filtered) and exposed to UV light for 15 min to form Trolox quinone. DNA ligands with Atto643 (Eurofins) were diluted to 1.5 nM in the Trolox-containing buffer and flushed into the sample chambers. A separate sample was used for every ligand to avoid signal contamination by ligands of different lengths. The excitation and detection paths were the same as in the widefield experiment except for the use of a broad band-pass filter (ET706/95m, Chroma) instead of a long-pass filter, and instead of the camera a SPAD (SPCM-AQRH-15, Excelitas, QY 70% at 700 nm) was used in combination with a TimeHarp 260 NANO Dual time tagger (PicoQuant). The signal from a single AuNR was projected onto the SPAD and photon arrival times were placed into bins of the desired duration.

Quantifying dynamics of blinking. Timetraces with 10 μs binning time were processed by the same event detection algorithm described above, allowing a maximum of 100 ms dark time for event merging. Events with a duration > 50 ms and a PCR $> 4 * 10^6$ photons/s were analyzed for blinking. The distribution of PCR values within an event was fitted to a double Gaussian (one for the on state and one for the off state). A threshold was set based on the minimum in this distribution and the duration of states above and below this threshold was analyzed.

Quantifying dynamics of monovalent ligands. Timetraces with 10 μs binning time were again processed by the event detection algorithm, where the allowed dark time was now set to 10, 5, 2, 1, 0.5, or 0.1 ms for 9nt, 8nt, 7nt, 6nt, 5nt, or noncomplementary ligands, respectively. To prevent artifacts due to separate short events being merged, events with a median PCR below threshold were discarded. The time between start and end of every event was then analyzed and processed into CDFs which were fitted with a double exponential.

Quantifying dynamics of multivalent (Holliday junction) ligands. The HJ strand carrying Atto643 was purchased from Eurofins; all other HJ strands were purchased from Integrated DNA Technologies. HJs were assembled by mixing the four strands (R, X, B, and H; see Supplementary Table S1) at equimolar concentrations in PBS, heating to 70°C, and cooling linearly to 4°C over 90 minutes. The HJ constructs were analyzed by 12% Native PAGE using 200V for 2h with 1xTBE as running buffer and appr. 0.5 pmol of HJ construct. The PAGE gel was made from 40% Accugel (National Diagnostics) and was stained with Sybr Gold (Invitrogen). Invitrogen UltraLow range DNA ladder was used as a reference. The gel was stained and imaged with an Amersham Typhoon laser scanner (see Supplementary Figure S12).

Trolox was added to TAE buffer (40 mM Tris-HCl, 20 mM acetic acid, 1 mM EDTA) with 10 mM $MgCl_2$, in the same way as described above. The HJs were then diluted to 1 nM in this buffer. The solution was flushed into the sample chambers and the measurements were performed in the same way as those on monovalent ligands.

Autocorrelation curves were produced by applying the Matlab function autocorr to the 10 μs binned timetraces, and fitted to a stretched exponential.

Numerical simulations of fluorescence enhancement. Simulations of AuNR plasmon resonances and fluorescence enhancement were performed with the boundary element method (BEM), using the MNPBEM17 toolbox [53]. AuNRs were approximated as cylinders capped by hemispheres. The dielectric function of gold was set to the values tabulated by Johnson & Christy. [54] The refractive index of the medium was set to 1.33 and the simulations neglected the effect of the substrate. The excitation wave with wavelength 637 nm was polarized along the AuNR long axis. Decay rate enhancements were computed across the dye's full emission spectrum, and combined with the intrinsic emission amplitudes following the approach of ref. [55]. More details are given in Supplementary Section S1.

References

1. Eisenmesser, E. Z. *et al.* Intrinsic dynamics of an enzyme underlies catalysis. *Nature* **438,** 117–121 (2005).
2. Acevedo-Rocha, C. G. *et al.* Pervasive cooperative mutational effects on multiple catalytic enzyme traits emerge via long-range conformational dynamics. *Nat. Commun.* **12,** 1–13 (2021).
3. Chowdhury, A., Nettels, D. & Schuler, B. Interaction Dynamics of Intrinsically Disordered Proteins from Single-Molecule Spectroscopy. *Annu. Rev. Biophys.* **52,** 433–462 (2023).
4. Liu, W. *et al.* Visualizing single-molecule conformational transition and binding dynamics of intrinsically disordered proteins. *Nat. Commun.* **14,** 1–12 (2023).
5. McKinney, S. A., Déclais, A. C., Lilley, D. M. & Ha, T. Structural dynamics of individual Holliday junctions. *Nat. Struct. Biol.* **10,** 93–97 (2003).
6. Ding, J. *et al.* Visualizing RNA conformational and architectural heterogeneity in solution. *Nat. Commun.* **14** (2023).
7. Maslov, I. *et al.* Sub-millisecond conformational dynamics of the A2A adenosine receptor revealed by single-molecule FRET. *Commun. Biol.* **6,** 1–15 (2023).
8. Stevers, L. M., de Vink, P. J., Ottmann, C., Huskens, J. & Brunsveld, L. A Thermodynamic Model for Multivalency in 14-3-3 Protein-Protein Interactions. *J. Am. Chem. Soc.* **140,** 14498–14510 (2018).
9. Ganser, L. R., Kelly, M. L., Herschlag, D. & Al-Hashimi, H. M. The roles of structural dynamics in the cellular functions of RNAs. *Nat. Rev. Mol. Cell Biol.* **20,** 474–489 (2019).
10. Eaton, W. A. Modern Kinetics and Mechanism of Protein Folding: A Retrospective. *J. Phys. Chem. B* **125,** 3452–3467 (2021).
11. Alberti, S. & Hyman, A. A. Biomolecular condensates at the nexus of cellular stress, protein aggregation disease and ageing. *Nat. Rev. Mol. Cell Biol.* **22,** 196–213 (2021).

12. Huttlin, E. L. *et al.* Architecture of the human interactome defines protein communities and disease networks. *Nature* **545,** 505–509 (2017).

13. Uversky, V. N. Intrinsically disordered proteins and their "Mysterious" (meta)physics. *Front. Phys.* **7,** 8–23 (2019).

14. Wu, S. *et al.* Kinetics of the conformational cycle of Hsp70 reveals the importance of the dynamic and heterogeneous nature of Hsp70 for its function. *Proc. Natl. Acad. Sci. U. S. A.* **117,** 7814–7823 (2020).

15. Van Loenhout, M. T., De Grunt, M. V. & Dekker, C. Dynamics of DNA supercoils. *Science* **338,** 94–97 (2012).

16. Pradhan, B. *et al.* The Smc5/6 complex is a DNA loop-extruding motor. *Nature* **616,** 843–848 (2023).

17. Metskas, L. A. & Rhoades, E. Single-molecule FRET of intrinsically disordered proteins. *Annu. Rev. Phys. Chem.* **71,** 391–414 (2020).

18. Riera, R. *et al.* Single-molecule imaging of glycan-lectin interactions on cells with Glyco-PAINT. *Nat. Chem. Biol.* **17,** 1281–1288 (2021).

19. Marzano, N. R., Paudel, B. P., Oijen, A. M. V. & Ecroyd, H. Real-time single-molecule observation of chaperone- assisted protein folding. *Sci. Adv.* **8,** eadd0922 (2022).

20. Tas, R. P., Hendrix, M. M. R. M. & Voets, I. K. Nanoscopy of single antifreeze proteins reveals that reversible ice binding is sufficient for ice recrystallization inhibition but not thermal hysteresis. *Proc. Natl. Acad. Sci.* **120,** 2017 (2023).

21. Chung, H. S., McHale, K., Louis, J. M. & Eaton, W. A. Single-molecule fluorescence experiments determine protein folding transition path times. *Science* **335,** 981–984 (2012).

22. Tsukanov, R., Tomov, T. E., Berger, Y., Liber, M. & Nir, E. Conformational Dynamics of DNA Hairpins at Millisecond Resolution Obtained from Analysis of Single-Molecule FRET Histograms. *J. Phys. Chem. B* **117,** 16105–16109 (2013).

23. Wang, J. *et al.* Gaussian accelerated molecular dynamics: Principles and applications. *Wiley Interdiscip. Rev. Comput. Mol. Sci.* **11,** 1–32 (2021).

24. Verschueren, D. V. *et al.* Label-Free Optical Detection of DNA Translocations through Plasmonic Nanopores. *ACS Nano* **13,** 61–70 (2019).

25. Needham, L.-M. *et al.* Label-free observation of individual solution phase molecules, Preprint at https://www.biorxiv.org/content/10.1101/2023.03.24.534170v1.full (2023).

26. Baaske, M. D., Asgari, N., Punj, D. & Orrit, M. Nanosecond time scale transient optoplasmonic detection of single proteins. *Sci. Adv.* **8,** 1–8 (2022).

27. Tiwari, S., Roy, P., Claude, J.-b. & Wenger, J. Achieving High Temporal Resolution in Single-Molecule Fluorescence Techniques Using Plasmonic Nanoantennas. *Adv. Opt. Mater.* **11,** 2300168 (2023).

28. Huskens, J. *et al.* A model for describing the thermodynamics of multivalent host-guest interactions at interfaces. *J. Am. Chem. Soc.* **126,** 6784–6797 (2004).

29. Lu, X., Ye, G., Punj, D., Chiechi, R. C. & Orrit, M. Quantum Yield Limits for the Detection of Single-Molecule Fluorescence Enhancement by a Gold Nanorod. *ACS Photonics* **7,** 2498–2505 (2020).

30. Puchkova, A. *et al.* DNA Origami Nanoantennas with over 5000-fold Fluorescence Enhancement and Single-Molecule Detection at 25 μm. *Nano Lett.* **15,** 8354–8359 (2015).

31. Wientjes, E., Renger, J., Cogdell, R. & Van Hulst, N. F. Pushing the Photon Limit: Nanoantennas Increase Maximal Photon Stream and Total Photon Number. *J. Phys. Chem. Lett.* **7,** 1604–1609 (2016).

32. Wang, Y., Horáček, M. & Zijlstra, P. Strong Plasmon Enhancement of the Saturation Photon Count Rate of Single Molecules. *J. Phys. Chem. Lett.* **11,** 1962–1969 (2020).

33. Nikoobakht, B. & El-Sayed, M. A. Preparation and growth mechanism of gold nanorods (NRs) using seed-mediated growth method. *Chem. Mater.* **15,** 1957–1962 (2003).

34. Katz-Boon, H. *et al.* Three-dimensional morphology and crystallography of gold nanorods. *Nano Lett.* **11,** 273–278 (2011).

35. Koenderink, A. F. Single-Photon Nanoantennas. *ACS Photonics* **4,** 710–722 (2017).

36. Sönnichsen, C. *et al.* Drastic reduction of plasmon damping in gold nanorods. *Phys. Rev. Lett.* **88,** 774021–774024 (2002).

37. Liu, M., Guyot-Sionnest, P., Lee, T. W. & Gray, S. K. Optical properties of rodlike and bipyramidal gold nanoparticles from three-dimensional computations. *Phys. Rev. B - Condens. Matter Mater. Phys.* **76,** 1–10 (2007).

38. Horáček, M., Engels, D. J. & Zijlstra, P. Dynamic single-molecule counting for the quantification and optimization of nanoparticle functionalization protocols. *Nanoscale* **12,** 4128–4136 (2020).

39. Caldarola, M., Pradhan, B. & Orrit, M. Quantifying fluorescence enhancement for slowly diffusing single molecules in plasmonic near fields. *J. Chem. Phys.* **148,** 123334 (2018).

40. Mertens, H. & Polman, A. Strong luminescence quantum-efficiency enhancement near prolate metal nanoparticles: Dipolar versus higher-order modes. *J. Appl. Phys.* **105,** 044302 (2009).

41. Cordes, T., Vogelsang, J. & Tinnefeld, P. On the Mechanism of Trolox as Antiblinking and Antibleaching Reagent. *J. Am. Chem. Soc.* **131,** 5018–5019 (2009).

42. Nooteboom, S. W., Wang, Y., Dey, S. & Zijlstra, P. Real-Time Interfacial Nanothermometry Using DNA-PAINT Microscopy. *Small* **18,** 2201602 (2022).

43. Jungmann, R. *et al.* Single-Molecule Kinetics and Super-Resolution Microscopy by Fluorescence Imaging of Transient Binding on DNA Origami. *Nano Lett.* **10,** 4756–4761 (2010).

44. Schueder, F. *et al.* An order of magnitude faster DNA-PAINT imaging by optimized sequence design and buffer conditions. *Nat. Methods* **16,** 1101–1104 (2019).

45. Alavijeh, H. N. & Baltus, R. E. Can Hindered Transport Models for Rigid Spheres Predict the Rejection of Single Stranded DNA from Porous Membranes? *Membranes (Basel).* **12,** 1–15 (2022).

46. Mammen, M., Choi, S. K. & Whitesides, G. M. Polyvalent interactions in biological systems: Implications for design and use of multivalent ligands and inhibitors. *Angew. Chemie - Int. Ed.* **37,** 2754–2794 (1998).

47. Fasting, C. *et al.* Multivalency as a chemical organization and action principle. *Angew. Chemie - Int. Ed.* **51,** 10472–10498 (2012).

48. Martinez-Veracoechea, F. J. & Frenkel, D. Designing super selectivity in multivalent nano-particle binding. *Proc. Natl. Acad. Sci. U. S. A.* **108,** 10963–10968 (2011).

49. Bergkamp, M. H., Van IJzendoorn, L. J. & Prins, M. W. Real-Time detection of state transitions in stochastic signals from biological systems. *ACS Omega* **6,** 17726–17733 (2021).

50. Shaw, A. *et al.* Binding to nanopatterned antigens is dominated by the spatial tolerance of antibodies. *Nat. Nanotechnol.* **14,** 184–190 (2019).

51. Spratt, J. *et al.* Multivalent insulin receptor activation using insulin-DNA origami nanostructures. *Nat. Nanotechnol.* (2023).

52. Horáček, M., Armstrong, R. E. & Zijlstra, P. Heterogeneous Kinetics in the Functionalization of Single Plasmonic Nanoparticles. *Langmuir* **34,** 131–138 (2018).

53. Hohenester, U. & Trügler, A. MNPBEM - A Matlab toolbox for the simulation of plasmonic nanoparticles. *Comput. Phys. Commun.* **183,** 370–381. arXiv: 1109.5783 (2012).

54. Johnson, P. & Christy, R. Optical Constant of the Nobel Metals. *Phys. Rev. B* **6,** 4370–4379 (1972).

55. Ringler, M. *et al.* Shaping Emission Spectra of Fluorescent Molecules with Single Plasmonic Nanoresonators. *Phys. Rev. Lett.* **100,** 203002 (2008).